(20)

LUNAR RADARGRAMMETRY WITH ALSE-VHF IMAGERY

Dr. Franz Leberl
NAS-NRC Resident Research Associate
Jet Propulsion Laboratory
California Institute of Technology
4800 Oak Grove Drive
Pasadena, California 91103

BIOGRAPHICAL SKETCH

Franz Leberl graduated in 1967 as a geodetic "diploma engineer" from the Technical University of Vienna, Austria. After Military service in Austria in 1968 he joined the scientific staff of the International Institute for Aerial Survey and Earth Sciences (ITC), Netherlands, in 1969. In 1972 he obtained a doctorate from the Technical University of Vienna, Austria. His research concerned geometric aspects of nonconventional imaging sensors, interpolation techniques, digital terrain models, and reseau photography.

ABSTRACT

Satellite radar will be available in the near future for imaging both the Earth and other planets. So far, the feasibility of Side-Looking Orbital Radar (SLOR) has been demonstrated only once, in the Apollo Lunar Sounder Experiment (ALSE) of the Apollo 17 mission to the Moon in December 1972. A pair of overlapping Apollo 17 synthetic aperture radar images (wavelength 2 m), produced during two consecutive orbits of the command module, is used for a radargrammetric evaluation of the potential of this imagery. The main purpose of this evaluation is to demonstrate the possibilities and limitations of satellite radar imagery for radargrammetric work. The paper presents some first results of the evaluation, which indicate that the height accuracy obtained with this imagery is superior to that obtained with the vidicon camera that is presently used for planetary exploration.

1. INTRODUCTION

The first civilian imaging Side-Looking Orbital Radar (SLOR) system was not placed in orbit around the Earth, but around the Moon on board the command module of Apollo 17 in December 1972 (Phillips, et al., 1973). The radar system was used for the Apollo Lunar Sounder Experiment (ALSE) and operated in three wavelengths of 60 m, 20 m (high frequency, HF) and 2 m (very high frequency, VHF). The main purpose of the experiment was to procure radar profiles, possibly for the analysis of subsurface features. The 60-m wavelength radar in particular was intended to produce some data from up to 1 km below the lunar surface. However, the radar systems were designed in such a way that side-looking radar images were also produced.

For the purpose of mapping the lunar surface, only the shortest wavelength (VHF, 2-m) radar produced sufficient returns from features not lying along the spacecraft track (off-track). But even this wavelength

is very long compared to the conventional 0.8-cm or 3-cm wavelength imagery commonly produced from an airborne platform. However, wavelength in itself is of no effect on radargrammetry. It only defines the minimum roughness of the surface required to produce diffuse reflections of the electromagnetic energy. For example, with a 2-m wavelength, the surface will appear much smoother than with a 3-cm wavelength. Therefore, most returns received by the ALSE radar are specular reflections from crater walls. This is demonstrated in Fig. 1, which shows a pair of overlapping radar images of crater Maraldi and Mons Maraldi on the Moon (19°N, 35°E). Figure 2 shows a portion of a conventional metric photograph of the same area.

Side-looking orbital radar images of the earth will be produced from SEASAT-A in 1978, and are being planned for the Space Shuttle and the exploration of the planet Venus. It is, therefore, of interest to study the lunar satellite radar images for the purpose of identifying their

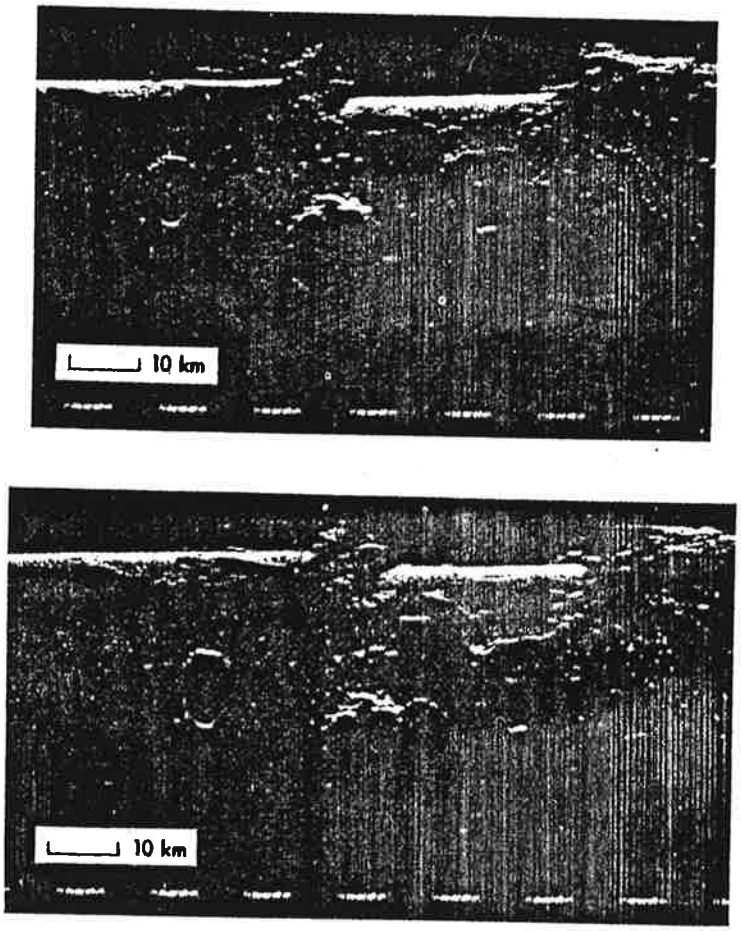

Fig. 1. ALSE-VHF side-looking orbital radar images of crater Maraldi on the Moon. Images were produced during revolutions 25 and 26 of the Apollo 17 command module

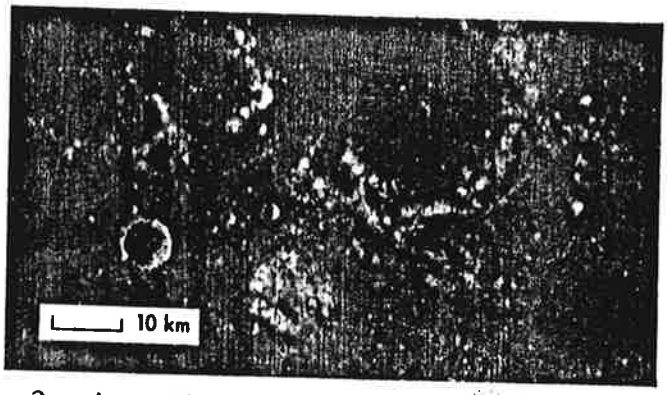

Fig. 2. A section of the Apollo 17 metric frame photograph No. 1495 of the crater and Mons Maraldi

adargrammetric possibilities and limitations. As a result, conclusions can be drawn with respect to both future orbital radar missions as well as the usefulness of ALSE imagery for mapping previously unmapped areas on the Moon.

The paper will present some first results obtained in a controlled experiment with a pair of overlapping ALSE-VHF images, produced in two consecutive revolutions of the Apollo 17 command module around the Moon. But prior to describing the test material, computations, and results, a theoretical section will treat the mathematical tools for ALSE radargrammetry.

2. MATHEMATICAL FORMULATIONS FOR ALSE RADARGRAMMETRY

2.1 Image Coordinates, Time, and Range

In the particular case of the ALSE-radar, imaging was done with a constant film transport velocity. Defining the image x coordinate in the along-track direction, one can easily relate, therefore, this x-coordinate to time t:

$$t = x/c_1 \qquad (1)$$

where c_1 is the constant film transport velocity. The ALSE-system splayed slant ranges without any further processing, so that an image y coordinate defined in the across-track direction is converted into slant range r by

$$r = (y/c_2 + c_3) \cdot c_0/2 \qquad (2)$$

where c_0 is the speed of electromagnetic radiation, c_3 is a constant sweep delay, and c_2 is the velocity of the flying spot across the screen of the radar display cathode ray tube. Equations (1) and (2) apply for the particular case of straight forward slant range presentation and constant film transport velocity. Other relations might apply to other radar systems.

2.2 Projection Equations

Time t relates the radar image to the orbit trajectory, which can be presented in a number of different ways. A very convenient form is with a position and velocity vector (position: $\underline{s} = (s_1, s_2, s_3)$; velocity: $\dot{\underline{s}} = (\dot{s}_1, \dot{s}_2, \dot{s}_3)$) of the spacecraft at time t, given in a coordinate system attached to the Moon and thus rotating with it (Fig. 3). Denoting the unknown position vector of a surface point by $\underline{p}$, one can write (Gracie, et al., 1970; Konecny, 1970; Leberl, 1972):

$$|\underline{p} - \underline{s}| = r \tag{3a}$$

$$\dot{\underline{s}} \cdot (\underline{p} - \underline{s}) = 0 \tag{3b}$$

Equation (3a) represents a sphere as the locus of points at slant range r from the antenna center. The two vertical bars (||) are used to define the length of a vector. Equation (3b) is a plane normal to the velocity vector, representing the locus of points with zero Doppler frequency.

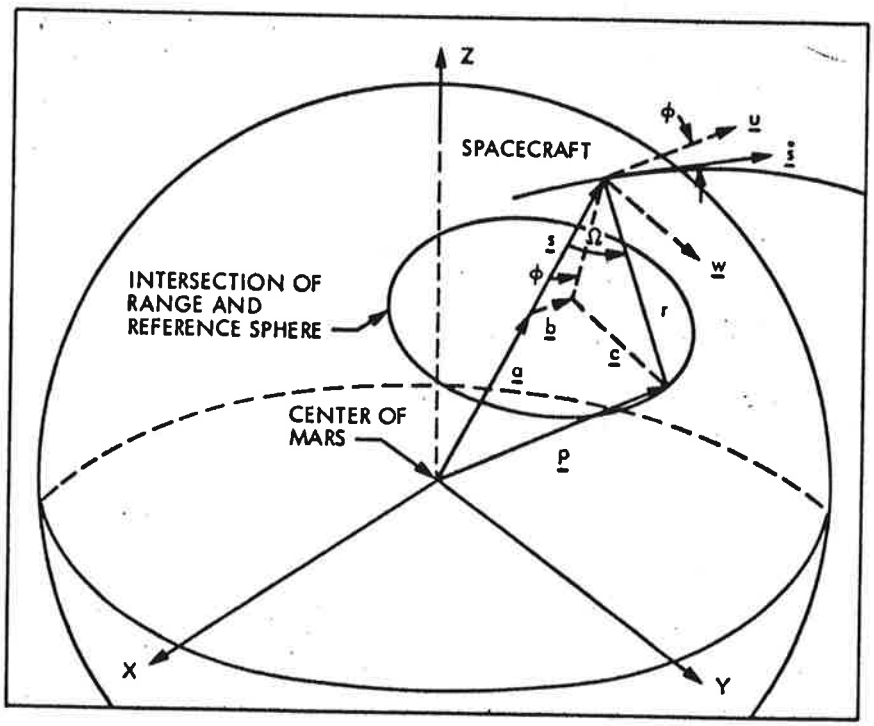

Fig. 3. Definition of the coordinate system and vectors relevant to radargrammetric computations. Vector $\underline{w}$ is normal on $\underline{s}$ and $\dot{\underline{s}}$; vector $\underline{u}$ is normal on $\underline{s}$ and $\underline{w}$. Vector $\underline{b}$ is parallel to $\underline{u}$, and $\underline{c}$ is parallel to $\underline{w}$

Instead of using Eqs. (3), vector $\underline{p}$ can be written as an explicit function of $\underline{s}$, $\dot{\underline{s}}$, and r. For this, however, a new unknown (elevation) angle Ω has to be introduced in a vector $\underline{q}$, so that:

$$\underline{q} = r \cdot (0, \sin\Omega, \cos\Omega)^T \tag{4a}$$

$$\underline{p} = \underline{s} + \underline{A} \cdot \underline{q} \tag{4b}$$

Rotation Matrix $\underline{A}$ contains the velocity vector $\dot{\underline{s}} = (\dot{s}_1, \dot{s}_2, \dot{s}_3)$:

$$a_{11} = \dot{s}_1/\dot{s} \qquad a_{21} = +\dot{s}_2/\dot{s}$$

$$a_{12} = -\dot{s}_2/\dot{s}_p \qquad a_{22} = \dot{s}_1/\dot{s}_p$$

$$a_{13} = +\dot{s}_1 \cdot \dot{s}_3/(\dot{s} \cdot \dot{s}_p) \qquad a_{23} = -\dot{s}_2 \cdot \dot{s}_3/(\dot{s} \cdot \dot{s}_p)$$

$$a_{31} = \dot{s}_3/\dot{s} \qquad a_{32} = 0$$

$$a_{33} = \dot{s}_p/\dot{s}$$

with

$$\dot{s}_p = \sqrt{\dot{s}_1^{\,2} + \dot{s}_2^{\,2}}; \quad \dot{s} = |\dot{\underline{s}}|$$

2.3 Mapping with a Single Orbital Radar Image

Mapping with a single orbital radar image means the reprojection of the image onto the reference figure, namely a sphere (or ellipsoid). Reprojection is achieved by solving a pair of equations of type (3) together with the equation of the planetary reference figure with radius SR:

$$|\underline{p}| = SR \tag{5}$$

Formulations (3) and (5) would be preferable in the present context to (4) and (5), because they consist of only three equations with three unknowns per image point as opposed to four equations with four unknowns.

However, a much more efficient approach is based on Fig. 3. Inputs to this formulation are position vector $\underline{s}$ of the sensor, velocity vector $\dot{\underline{s}}$, radius SR of the reference sphere, and radius r of the range sphere. The reference figure and range sphere intersect along a plane perpendicular to the position vector $\underline{s}$ and a distance $a = |\underline{a}|$ from the origin. The plane is thus defined by vector $\underline{a}$:

$$\underline{a} = \underline{s} \cdot a/s \tag{6a}$$

$$a = (SR^2 + s^2 - r^2)/2s \tag{6b}$$

Defining a pair of unit vectors $\underline{u}$, $\underline{w}$ by:

$$\underline{w} = (\dot{\underline{s}} \times \underline{s})/|\dot{\underline{s}} \times \underline{s}| \tag{7a}$$

$$\underline{u} = \underline{w} \times \underline{s}/|\underline{w} \times \underline{s}| \tag{7b}$$

and angle ϕ by:

$$\cos \phi = \underline{u} \cdot \dot{\underline{s}}/\dot{s} \tag{8}$$

one obtains vector $\underline{b}$ as:

$$\underline{b} = \underline{u} \cdot (s - a) \cdot \tan \phi \tag{9}$$

To define the position vector $\underline{p}$ of the point of intersection of the radar projection ray and the sphere, another auxiliary vector $\underline{c}$ is required:

$$\underline{c} = \underline{w} \cdot \left(r^2 - b^2 - (s - a)^2\right)^{1/2} \tag{10}$$

so that:

$$\underline{p} = \underline{a} + \underline{b} + \underline{c} \tag{11}$$

This formulation, in addition to being efficient, avoids ambiguities of imaging to the right or left by simply defining the direction of vector $\underline{w}$ appropriately. Other solutions using Eqs. (5), (3), or (4) all produce an ambiguous result when intersecting the circular radar projection ray with a sphere.

2.4 Formation of a Stereo Model

Formulation of a stereo model means the simultaneous solution of two pairs of Eqs. (3) with the 3 unknowns p_1, p_2, p_3:

$$\begin{aligned} |\underline{p} - \underline{s}'| &= r' \\ |\underline{p} - \underline{s}''| &= r'' \\ \dot{\underline{s}}' \cdot (\underline{p} - \underline{s}') &= 0 \\ \dot{\underline{s}}'' \cdot (\underline{p} - \underline{s}'') &= 0 \end{aligned} \tag{12}$$

This is an overdetermined set of nonlinear equations, which should be linearized for application of a least squares algorithm. One obtains:

$$\underline{C} \cdot \underline{v} + \underline{D} \cdot \underline{x} + \underline{w} = 0 \tag{13}$$

Vector $\underline{v}$ contains the corrections to the observations s'_1, s'_2, s'_3, $\dot{s}'_1$, $\dot{s}'_2$, $\dot{s}'_3$, s''_1, s''_2, s''_3, $\dot{s}''_1$, $\dot{s}''_2$, $\dot{s}''_3$, r', and r''. Vector $\underline{x}$ contains corrections to the approximate values of the unknown $\underline{p} = (p_1, p_2, p_3)$.

$\underline{C}$ and $\underline{D}$ are coefficient matrices. Vector $\underline{w}$ contains the contradictions. The unknown $\underline{x}$ and their variance-covariance matrix $\underline{Q}_x$ are obtained as:

$$\underline{x} = -(\underline{D}^T \cdot (\underline{C} \cdot \underline{G}^{-1} \cdot \underline{C}^T)^{-1} \cdot \underline{D})^{-1} \cdot \underline{D}^T \cdot (\underline{C} \cdot \underline{G}^{-1} \cdot \underline{C}^T)^{-1} \cdot \underline{w} \quad (14a)$$

$$\underline{Q}_x = (\underline{D}^T \cdot (\underline{C} \cdot \underline{G}^{-1} \cdot \underline{C}^T)^{-1} \cdot \underline{D})^{-1} \quad (14b)$$

$\underline{G}$ is the weight matrix of the observations.

Instead of using Eq. (3) for the formation of a stereo model, formulation of a coplanarity condition is possible by equating two sets of Eq. (4):

$$\underline{A} \cdot \underline{u}' + \underline{s}' - \underline{s}'' - \underline{A}'' \cdot \underline{u}'' = 0 \quad (16)$$

This is a set of three equations with two unknown Ω' and Ω''. Linearization leads to:

$$\underline{E} \cdot \underline{x} + \underline{w} = \underline{v} \quad (17)$$

where $\underline{x} = (d\Omega', d\Omega'')$ is the vector of corrections to the approximate values of the unknown. Finally:

$$\underline{x} = -(\underline{E}^T \cdot \underline{G} \cdot \underline{E})^{-1} \cdot \underline{E}^T \cdot \underline{G} \cdot \underline{w} \quad (18)$$

Formulation (18) does not minimize the square sum of observational errors, but the distance between projection rays. Vector $\underline{v}$ contains the elements v_X, v_Y, v_Z of the minimum distance between the projection rays.

2.5 Simplified Formulations

For part of a planetary surface of limited extent, a simplified formulation can be found for mapping with a single radar image as well as formulation of a stereo model.

Approximating the orbits by straight line elements parallel to the surface, which is assumed to be plane, one obtains for a single image:

$$\begin{aligned} X &= x \cdot sc \\ Y &= (r^2 - H^2)^{1/2} \end{aligned} \quad (19)$$

and for a stereo pair (see Fig. 4):

$$\begin{aligned} X &= (x' \cdot sc + x'' \cdot sc)/2 \\ Y &= (r''^2 - r'^2 - B^2)/(2 \cdot B) \\ Z &= H - (r'^2 - Y^2)^{1/2} \end{aligned} \quad (20)$$

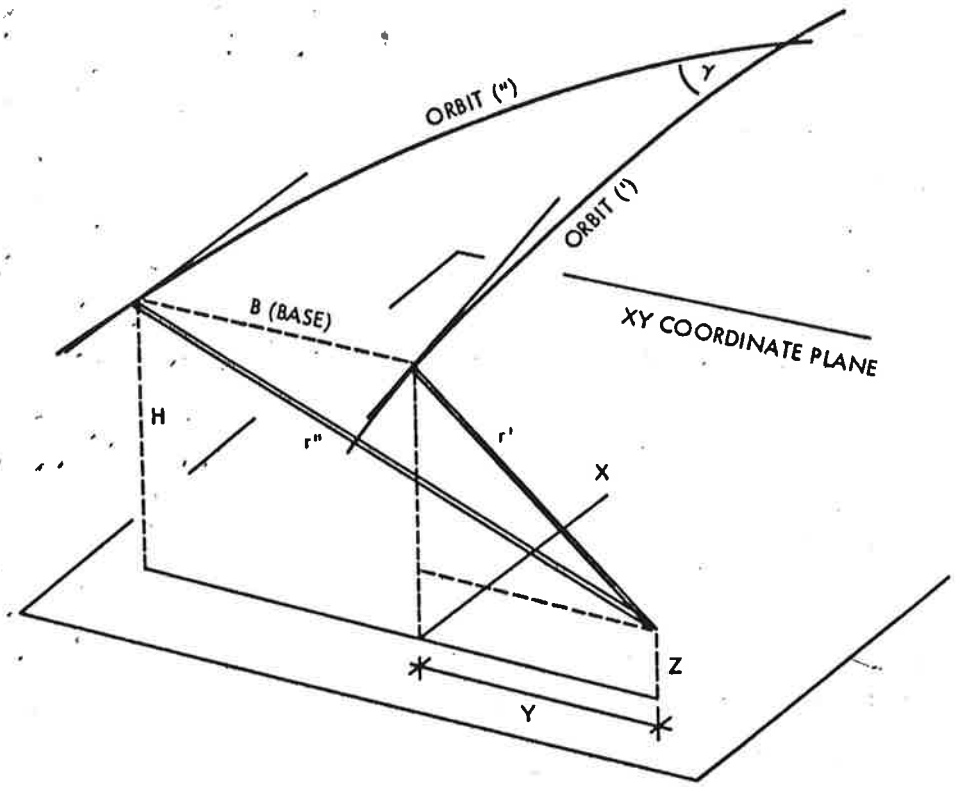

Fig. 4. Explanation of entities for simplified formulation of lunar radargrammetry. The two orbits converge with an angle γ (this is ~ 2° in the case of Apollo 17). The orbits are locally approximated by straight lines, and a local rectangular X, Y, Z coordinate system is defined

where H is the altitude of the radar system above the surface, B is the base (distance between the two orbits), and the Y-coordinate is in a locally defined orthogonal coordinate system with the X-axis parallel to the orbit. Figure 4 shows that the stereo base B is variable along the orbit. Its maximum is at the equator, and, in the vicinity of the maximum latitude, the base is zero. B has therefore to be computed from the nominal orbit inclination, orbital period, planetary rotation, and planetographic location of the area of interest.

2.6 Use of Ground Control Points

Two different approaches are formulated for the adjustment of ALSE-VHF radar data to known ground control. These approaches can be parametric or interpolative (Leberl, 1972; Baker, et al., 1975).

In the interpolative case, the transformation of the radar coordinates into the reference coordinate system proceeds without use of external point controls. However, differences $\underline{d}$ are encountered between the

radargrammetrically defined vector $\underline{p}$ and the known ground control point vector $\underline{g}$:

$$\underline{d} = \underline{g} - \underline{p} \qquad (21)$$

These differences are approximated by an interpolative procedure, e.g., a moving average or linear prediction, to correct radargrammetric points.

In the parametric formulation, an approach by Gracie, et al., (1970) is used in a slightly modified form. The observed orbit is intercepted at point $\underline{s}$ by a zero-Doppler plane through each ground control point (Fig. 5). Representing the orbit by linear pieces, beginning at point $\underline{s}_i$ and oriented along vector $\dot{\underline{s}}_i$, the zero-Doppler plane passes through the control point defined by vector $\underline{g}$ and is perpendicular to the orbit piece i. Therefore, the distance e between the end points of vectors $\underline{s}$ and $\underline{s}_i$ is the minimum distance between $\underline{s}_i$ and the zero Doppler plane. Thus:

$$e = \dot{\underline{s}}_i \cdot (\underline{s}_i - \underline{g})$$

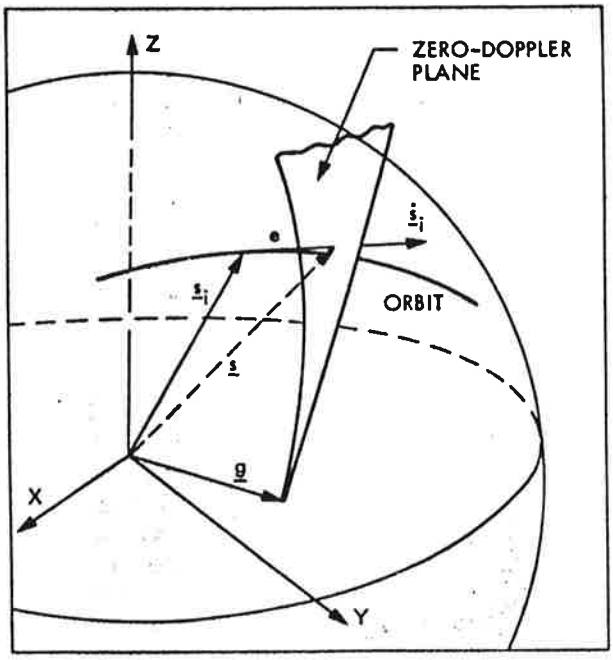

Fig. 5. Intersection of zero-Doppler plane and orbit if the ground control point with position vector $\underline{g}$ is given. Vector $\underline{s}$ is the position vector of the point of intersection, $\dot{\underline{s}}_i$ the velocity vector, and $\underline{s}_i$ the position vector defining a linear piece of the orbit

so that:

$$\underline{s} = \underline{s}_i + \dot{\underline{s}}_i \cdot e/\dot{s}_i \tag{22}$$

With vector $\underline{s}$ the slant range r_g and time t_g of imaging ground control point g can easily be found. The radar image itself also produces values for r and t. The differences dr and dt,

$$\begin{aligned} dr &= r_g - r \\ dt &= t_g - t \end{aligned} \tag{23}$$

can be used to calibrate the radargrammetric time and range measurements. It is proposed that this calibration be done with the following polynominals:

$$dr = a_0 + a_1 \cdot x + a_2 \cdot x^2 + a_3 \cdot x^3 + a_4 \cdot y + a_5 \cdot x \cdot y + a_6 \cdot x^2 \cdot y + \cdots \tag{24a}$$

$$dt = b_0 + b_1 \cdot x + b_2 \cdot x^2 + b_3 \cdot x^3 + \cdots \tag{24b}$$

The form of polynominal (24a) is chosen linear in the cross-track direction. One neither expects nonlinear variation of dr from differentiating Eq. (2), nor from past experiences (Gracie, et al., 1970). In orbit direction, image coordinate errors vary because of an erroneous orbit similar to airborne radar. Therefore, calibration polynomials have to be chosen that are of higher order or piecewise in this direction. For a new radargrammetric point, slant range r, and time t are corrected with the calibration polynominals (24). The corrected time t is used to interpolate the orbit position and velocity vectors of a new point.

3. DESCRIPTION OF TEST MATERIAL AND PREPROCESSING

3.1 Measurements

Input to the radargrammetric evaluation of ALSE-VHF imagery is a pair of overlapping orbital radar strips over crater Maraldi, as shown in Fig. 1., and a stereo pair of Apollo 17 metric photography (frame Nos. 1495 and 1497; see Fig. 2). This particular area was selected for the study because it has surface relief that varies from smooth to mountainous (height differences in excess of 1000 m). A small stereo base of about 3 km allows for good stereo viewability. Radar projection rays intersect at angles of about 2°. This is very small indeed by photogrammetric standards, but leads to parallaxes sufficient to perceive a well defined radar stereo model.

About 70 points were identified in the radar and metric stereo models, pricked in the emulsion of the diapositives using a Wild-PUG point

transfer device (observed with 10X magnification), and were finally measured on a Mann monocomparator and an OMI Analytical Plotter (14X magnification). All measurements were carried out at the Center for Astrogeology of the U.S. Geological Survey in Flagstaff, Arizona. In addition to these identifiable, marked points, a digital height model of Mons Maraldi was measured in the metric and radar stereo models. For the latter, observation with a 6X magnification was found the best for good stereovision.

Table 1 summarizes relevant information about the images and measurements, whereas Fig. 6 illustrates the imaging configuration.

Table 1. Description of test material: ALSE-VHF radar and Apollo 17 metric imagery

Metric photography		Radar Imagery	
Principal distance	75.842 mm	Orbital altitude	116 km
Scale	1:1,500,000	Stereobase	3 km
Photograph Nos.	AS 1495, 1497	Max elevation angle	22°
Overlap	60%	Min elevation angle	
Predicted height accuracy	±30 m	Theoretical	-22°
Rms discrepancy between comparator and stereo plotter models	±30 m	Practical	-5°
		Sweep delay	746.25 μs
Rms discrepancy between map and stereo model		Along-track scale	1:1,000,000
Planimetry	±300 m	Across-track slant range scale	1:210,000
Height	±100 m	Wavelength	2 m
Diameter of marked points	70 μm	Resolution (slant)	10 m
		Resolution (ground)	30 to 150 m
		Diameter of marked points	70 μm

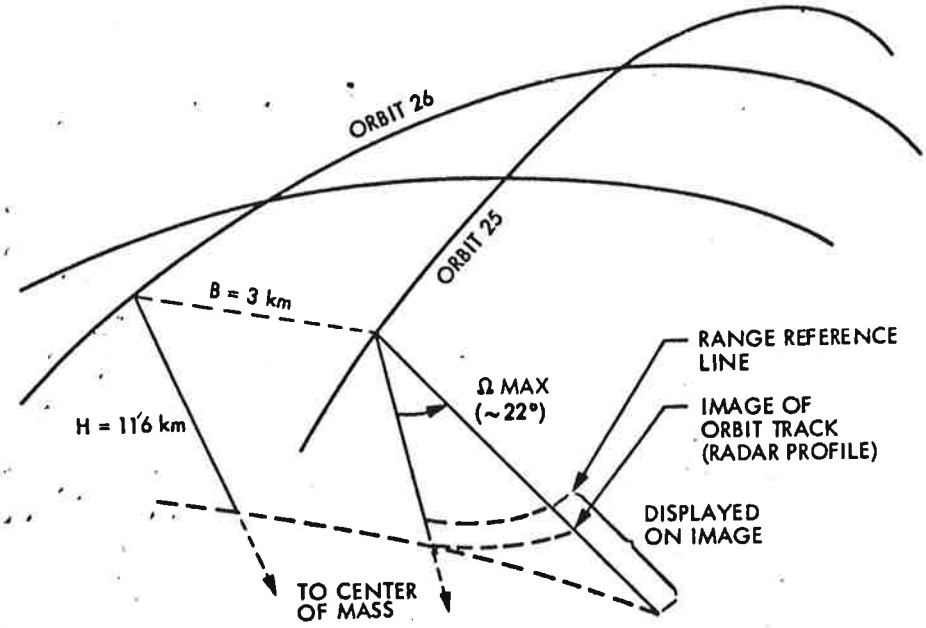

Fig. 6. Imaging configuration for ALSE-VHF radar, revolutions 25 and 26, over crater and Mons Maraldi

3.2 Preprocessing

Preprocessing consists of the photogrammetric reduction of the metric images and some preparation of the radar data. For the transformation of the metric stereo model into the lunar coordinate system, a set of lunar features were scaled off the 1:250,000 map. Surprisingly, residual differences between map and photogrammetric points amounted to ±300 m in planimetry, and ±100 m in height; discrepancies between the two independent photogrammetric measurements (on the Mann comparator and APC) are only ±30 m in all coordinate directions. This seems to indicate that the lunar map and limitations of identifying homologous points contributes the larger part of the above-mentioned residuals.

Radargrammetric preprocessing served to transform the comparator measurements into image coordinates, and to generate orbit data in a form appropriate for input to radargrammetry. The image coordinate axis x is defined along the range reference line generated electronically in the image. However, it unfortunately is not displayed in all optical correlations, specifically not in the ones of good image quality. Solution of this dilemma required identification and measurement of homologue points in different optical correlations of the same image. This allowed for the transfer of the range reference line into production imagery, and the evaluation of scale inconsistencies among different correlations of the same image.

Root mean square deviations of the range reference from a straight line are ±5 μm. This value proves that the range reference fulfills its purpose. Scale inconsistencies between different optical correlations

produced from the same signal film amount to more than 1% in the along-track direction. A similar number is also obtained for along-track scale differences between two different but overlapping images. This is in excess of what is being presently achieved in commercial airborne radar mapping (<0.5%; see Leberl, 1974).

However, time marks can eliminate the effect of along-track scale variations. Unfortunately, time marks generated during ALSE image acquisition were not well presented on the correlated map film (see Fig. 1). An attempt to use them, however, led to the conclusion that their relative spacing is quite consistent (error < 0.5%). The time marks would thus be perfectly well suited to relate the image with the orbit, if only their absolute position were accurately known.

4. RADARGRAMMETRIC RESULTS

4.1 Single Image Radargrammetry

Before going into actual ALSE results, an expected accuracy of mapping with single orbital ALSE images is presented in Fig. 7. This figure is obtained by formulating the propagation of errors of slant range r and orbital altitude H using Eq. (19). Since elevation angles of the line of sight are rather small for orbital images, large errors of the Y coordinate must be expected if the altitude above a feature is not well known.

This obvious expectation is confirmed by Table 2, which presents a summary of the radargrammetric results with a single radar image. Five transformations of the radar image coordinates into the lunar coordinate system were evaluated: (1) the simplified approach with

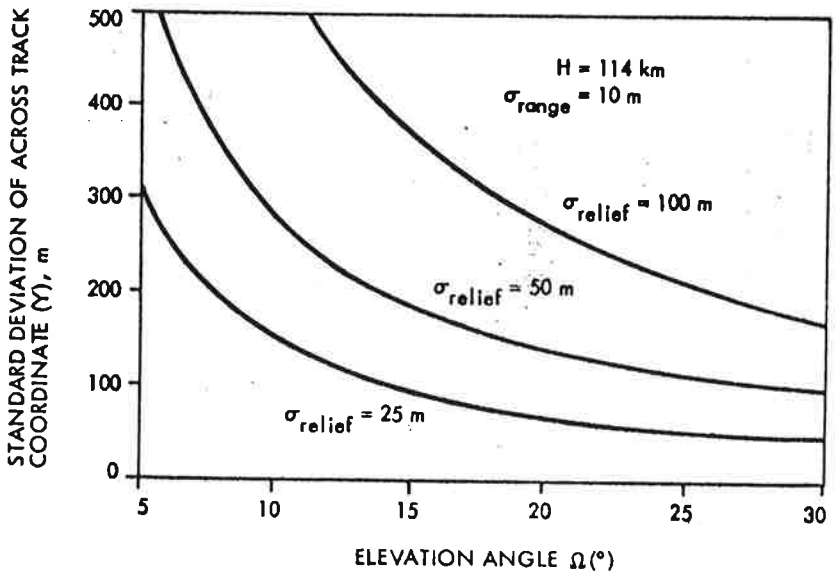

Fig. 7. Expected standard deviation of the across-track coordinate (Y) in single image ALSE radargrammetry

Table Summary of results from single-image radargrammetry[a]

Row	Orbit	Eqs. used	No. of control points	Rms X (m)	Rms Y (m)	Rms variation of radius vector (m)	No. of check points
i	Av altitude	(19)	2	320	670	120	49
ii	Av altitude	(19)	8	152	360	120	49
iii	Predicted orbit	(6) to (11)	0	2010	9700	120	49
iv	Predicted orbit	(6) to (11)	2	330	579	120	49
v	Predicted orbit	(6) to (11)	8	132	358	120	49
vi	Range and time calibration	(22), (24), (6) to (11)	1	451	415	120	49
vii	Range and time calibration	(22), (24), (6) to (11)	2	276	409	120	49
viii	Range and time calibration	(22), (24), (6) to (11)	8	160	362	120	49
ix	Range and time calibration	(22), (24), (6) to (11)	1	660	2240	235	65
x	Range and time calibration	(22), (24), (6) to (11)	1	147	233	56	18
xi[b]	Av altitude	(19)	Image comparison	75	175	120	49

[a] Values are root mean square discrepancies (m) between radar and stereophotogrammetrically determined coordinates of four checkpoints.

[b] The values in this row are rms discrepancies between radargrammetric points derived independently from two overlapping radar images.

formulae (19), followed by a four-parameter similarity transformation of the obtained X, Y coordinates using two lunar ground control points (row i); (2) correcting the output of approach (1) using a number of ground control points and polynomials of the form (24) to interpolate corrections to radargrammetric coordinates (row ii); (3) using the orbit made available by the Johnson Space Center, but no ground control points, and implementing formulae (6) to (11) (row iii); (4) correcting the output of approach (2) using ground control points (rows iv, v); (5) using the available orbit and ground control to calibrate range and time coordinates according to formulae (22), (23), and (24), followed by application of formulae (6) to (11) (rows vi, vii, viii).

Table 2 is largely self-explanatory. Root mean square values refer to a rectangular left-hand X, Y, Z coordinate system centered at 19°N, 35.5°E with the X-axis in orbit direction and the Z-axis along the local normal. The largest portion of the errors is contributed by derivations of lunar features from the datum sphere and the limited accuracy in identifying features in both the radar and metric photographs. If surface features that are obviously far from the datum sphere are excluded from consideration, the cross-track (Y) coordinate errors drop significantly (see rows ix and x of Table 2).

The size of the coordinate errors is somewhat larger than those obtained by Tiernan, et al., (1975) with the same images (±250-m coordinate errors). The reason for this is the fact that Tiernan, et al., studied only a small number of 13 rather well identifiable craters in Mare Serenitatis, where the deviations of features from a chosen datum sphere are predictably minimal (only about ±27 m). However, row (x) showed that exclusive consideration of "perfect" points leads also in the present study to results that compare favorably to those of Tiernan's, et al., (1975).

With the use of ground control points, all methods approach the same level of accuracy. There is, however, a tendency for the interpolative approach to be superior to the parametric. This confirms conclusions obtained by Baker, et al., (1975) for multispectral airborne imagery. Row xi of Table 2 finally provides evidence that the limitation to ALSE-single-image accuracy is set by the limitation in identifying details in the metric and radar images, and not by geometric weakness of the radar.

An interesting result is obtained in the range and time calibration performed for rows vi to viii. Figure 8 clearly shows that the time marks produce a rather erroneous relationship between the image and the orbit. This is the reason why row iii displays such large coordinate errors.

4.2 Stereoradargrammetry

Stereoradargrammetric results are so far available only from the simplified approach using formulae (20). Table 3 presents the overall result. A best fit of radar and metric stereo models using a conformal 7-parameter transformation (rotations and shifts) results in an overall height accuracy of ±280 m. Correcting the stereo model with up to 8 ground control points reduces this height error to ±120 m.

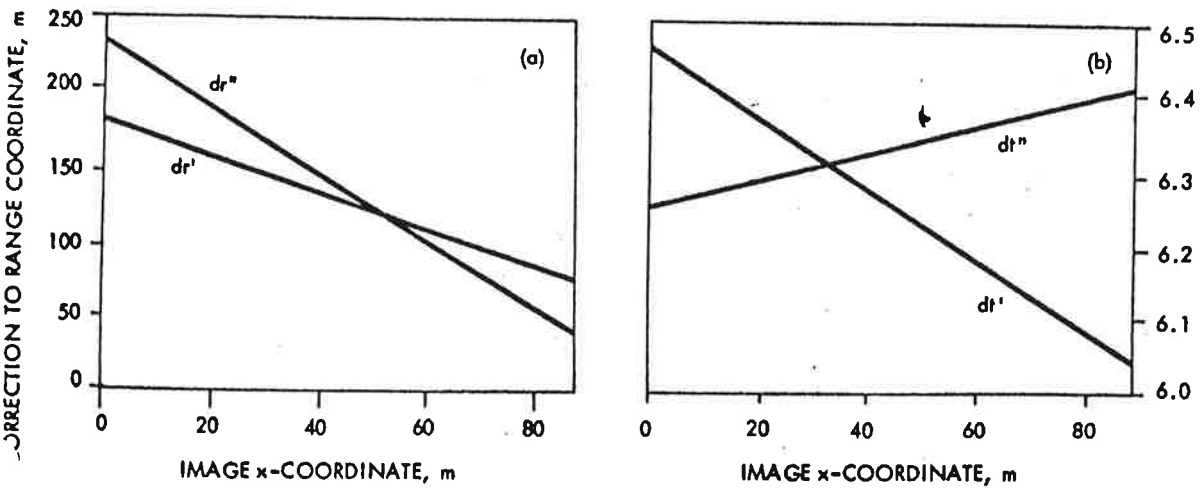

Fig. 8. Linear calibration function for range (a) and time (b) coordinates plotted as a function of image x-coordinate

Although height is rather accurately determined, the across-track coordinate (Y) is not. This can also be theoretically predicted from error propagation using Eqs. (20). Its results are shown as Fig. 9.

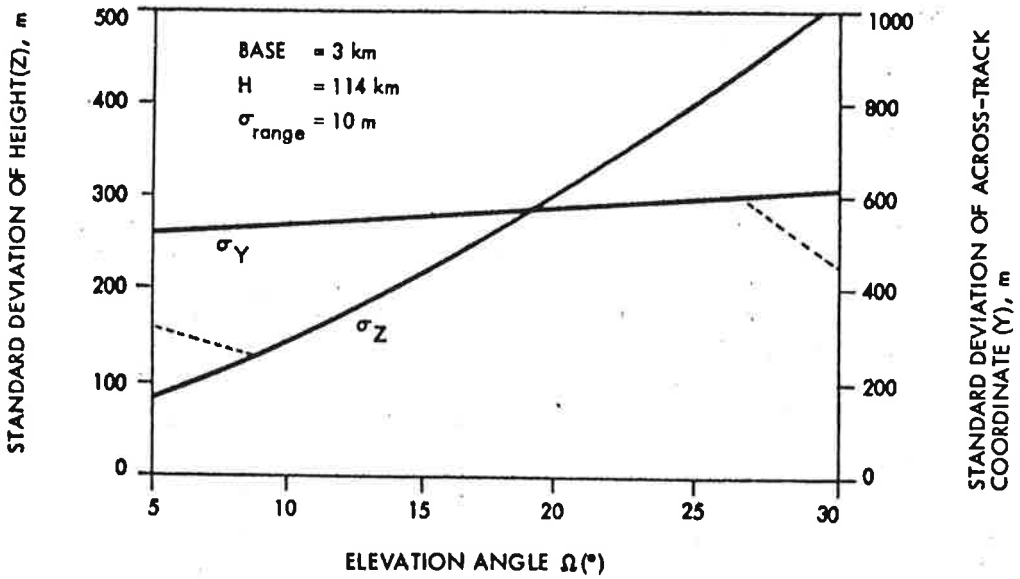

Fig. 9. Expected standard deviation of height (Z) and across-track coordinate (Y) derived from ALSE stereoradargrammetry. Values are computed from error propagation based on Eq. (20)

An interesting result is the determination of the depth of five craters of which rim and bottom could be identified. The depth of these craters was determined with a rms discrepancy of ±80 m between stereoradar- and stereophotogrammetry (see Table 4).

Table 3. Summary of preliminary results from stereoradargrammetry[a]

Row	Orbit	Eqs. used	No. of ground control points	Rms X (m)	Rms Y (m)	Rms Z (m)	No. of check points
i[b]	Av altitude and base	(20)	All	448	620	283	65
ii[b]	Av altitude and base	(20)	4	434	658	350	65
iii[b]	Av altitude and base	(20)	8	464	673	289	65
iv[c]	Av altitude and base	(20)	4	136	543	350	65
v[c]	Av altitude and base	(20)	8	130	506	121	65

[a] Values are root mean square discrepancies (m) between radar and stereophotogrammetrically determined coordinates of about 70 checkpoints.

[b] For these rows, a conformal best fit of the radar and metric models is computed, but no corrective deformation is applied to the radar model.

[c] For these rows, the 4 and 8 control points are used to compute correction polynomials.

Table 4. Crater depth measured from metric and radar stereo models

Parameter	Crater No.					RMS(m)
	1	2	3	4	5	
Depth from metric (m)	173	327	58	297	216	
Depth from radar (m)	135	205	105	328	103	
Difference (m)	38	122	-47	-31	113	±80

The digital height model of Mons Maraldi (see Fig. 1) was measured in the radar as well as metric stereo models, using the OMI Analytical Plotter as a stereo comparator. Intersecting a radar stereo model results in an irregular grid from which contour lines were interpolated using a moving average technique and standard computer contouring routine. Results are shown in Figures 10a and b. These contour plots are first results and illustrate that contouring is possible with orbital ALSE images. An obvious limitation of ALSE radar is that it imaged only the part of Mons Maraldi that slopes toward the orbit. As a consequence, half of the mountain cannot be contoured from radar. This, however, is largely a result of using a 2-m radar, where most reflections are specular on the lunar surface. Shorter wavelength radar would have enabled the production of a complete image of Mons Maraldi.

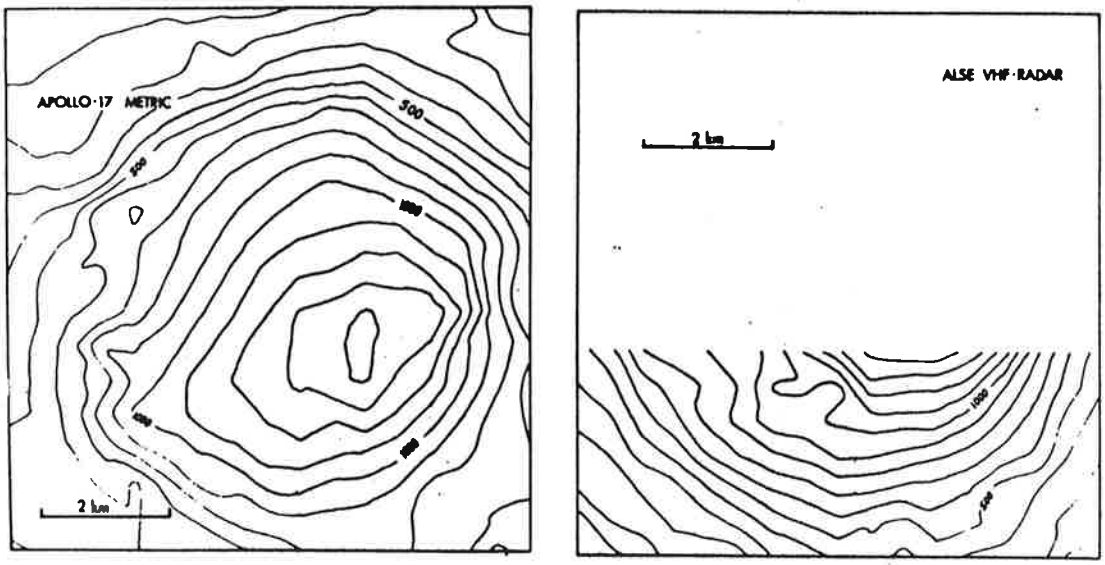

Fig. 10. Contour plots of Mons Maraldi procured from (a) Apollo 17 metric photography, and (b) ALSE-VHF stereoradar. Contour interval is 100 m

5. CONCLUSIONS

Lunar ALSE-VHF radar imagery was produced during two consecutive orbits of the Apollo 17 command module around the Moon. Evaluation of radargrammetric mapping with single strips and a radar stereo model led to preliminary results in a test area around Mons Maraldi. A number of different approaches was used to map from radargrammetric measurements in single and stereo pairs of radar images. Accuracy achieved with single radar images was about ±250 m along track and ±500 m across track (250 μm and 500 μm at image scale). These values are obtained by comparing radar and photogrammetrically reduced data from Apollo 17 metric photography. Accuracy is limited by the identifiability of corresponding details in the radar and metric images and the degree of smoothness of the imaged surface.

Stereoradargrammetry was used to generate a contour plot of Mons Maraldi and to evaluate the overall height accuracy obtainable from ALSE radar. The near vertical look angles used for orbital radar provide rather good height accuracy, even with small stereo bases. Planimetric accuracy, however, is reduced accordingly. A rather simple data reduction procedure led to a height accuracy of ±280 m without use of ground control. About ±120 m of accuracy are obtained if the stereo model is corrected using a few control points. This makes ALSE stereo radar heights competitive with, or even superior to, vidicon data obtained for planetary exploration (Blasius, 1973).

The basic limitation to radargrammetric accuracy from ALSE VHF images is the identifiability of surface features. Evidence is provided that the geometric strength of ALSE radar is superior to its potential to produce identifiable image details. Future orbital radar missions will presumably employ shorter wavelengths than the 2-m VHF. This should increase the amount and identifiability of surface features shown in the images.

ACKNOWLEDGMENTS

I am grateful to Mr. Sherman Wu and his colleagues of the Center for Astrogeology of the U. S. Geological Survey, Flagstaff, Arizona, for making available their equipment, time, and know-how for the radargrammetric and photogrammetric measurements. I am also indebted to Messrs. M. Tiernan and L. Roth of JPL for their help in solving many problems with the ALSE data and the Apollo 17 orbit parameters.

REFERENCES

Baker, J.R., G.W. Marks, E.M. Mikhail (1975), "Analysis of Digital Multispectral Scanner (MSS) Data," Bildmessung und Luftbildwesen, Vol. 43, No. 1, Karlsruhe, W. Germany.

Blasius, K. (1973), "A Study of Martian Topography by Analytic Photogrammetry," Journal of Geophysical Research, Vol. 78.

Derenyi, E.E. (1975), "Terrain Heights from SLAR Imagery," presented at the 41st Annual Meeting of the American Society of Photogrammetry, Washington, D.C., March 9 – 14.

Gracie, G., R. Brewer et al. (1970), Stereo Radar Analysis, Final Technical Report, Contract No. DACA 76-69-C-0002, ARPA Order No. 1229, Raytheon Automatic Operation.

Konecny, G. (1970), "Metric Problems in Remote Sensing," in Proceedings of the ISP-Comm IV Symposium, Delft, ITC-Publication, Series A, No. 50, Delft, Netherlands.

Leberl, F. (1972), "Evaluation of Single Strips of Side-Looking Radar Imagery," invited paper, Commission IV, 12th Congress of the International Society of Photogrammetry, Ottawa, Canada.

Leberl, F. (1974), "Evaluation of SLAR Image Quality and Geometry in PRORADAM," ITC Journal, Enschede, Netherlands, 1974/4.

Phillips, R., G.F. Adams et al. (1973), "Apollo Lunar Sounder Experiment," Apollo 17 Preliminary Science Report, NASA SP-330, Washington, D.C.

Lernan, M. et al. (1975), "Lunar Cartography with the Apollo 17 ALSE Radar Imagery", manuscript submitted to The Moon